

PAPER • OPEN ACCESS

## Towards *in-line real-time* characterization of roll-to-roll produced ZTO/Ag/ITO thin films by hyperspectral imaging

To cite this article: Susanne Dogan-Surmeier *et al* 2023 *J. Phys. D: Appl. Phys.* **56** 365102

View the [article online](#) for updates and enhancements.

You may also like

- [High-efficiency top-emitting organic light-emitting diodes based on metal/ITO composite electrodes](#)  
Ben Zhao, Jinzhi Pi, Jialu Gu et al.
- [Analyses of the light extraction efficiency of organic light-emitting diodes with ITO/mesh-Ag/ITO anode and its optical transmittance as transparent electrode](#)  
Kirak Kim, Eou-Sik Cho and Sang Jik Kwon
- [Possible Ohmic Mechanisms of Ag/Indium Tin Oxide p-Type Contacts for High-Brightness GaN -Based Light Emitting Diodes](#)  
June-O Song, Hyun-Gi Hong, Joon-Woo Jeon et al.

**PRIME**  
PACIFIC RIM MEETING  
ON ELECTROCHEMICAL  
AND SOLID STATE SCIENCE







**HONOLULU, HI**  
October 6-11, 2024

*Joint International Meeting of*  
The Electrochemical Society of Japan (ECSJ)  
The Korean Electrochemical Society (KECS)  
The Electrochemical Society (ECS)

Early Registration Deadline:  
**September 3, 2024**

**MAKE YOUR PLANS  
NOW!**

# Towards *in-line real-time* characterization of roll-to-roll produced ZTO/Ag/ITO thin films by hyperspectral imaging

Susanne Dogan-Surmeier<sup>1,6,\*</sup> , Florian Gruber<sup>3,6</sup> , Steffen Bieder<sup>1,6</sup>, Patrick Schlenz<sup>2</sup>, Michael Paulus<sup>1</sup>, Christian Albers<sup>1</sup> , Eric Schneider<sup>1</sup>, Nicola Thiering<sup>1</sup> , Christian Maurer<sup>4</sup>, Metin Tolan<sup>1,5</sup>, Philipp Wollmann<sup>3</sup> , Steffen Cornelius<sup>2</sup> and Christian Sternemann<sup>1,\*</sup> 

<sup>1</sup> Fakultät Physik/DELTA, Technische Universität Dortmund, Dortmund 44221, Germany

<sup>2</sup> Fraunhofer-Institut für Organische Elektronik, Elektronenstrahl- und Plasmatechnik FEP, Dresden 01277, Germany

<sup>3</sup> Fraunhofer-Institut für Werkstoff- und Strahltechnik IWS, Dresden 01277, Germany

<sup>4</sup> Bruker AXS GmbH, Karlsruhe 76187, Germany

<sup>5</sup> Georg-August-Universität Göttingen, Göttingen 37073, Germany

E-mail: [susanne.dogan@tu-dortmund.de](mailto:susanne.dogan@tu-dortmund.de) and [christian.sternemann@tu-dortmund.de](mailto:christian.sternemann@tu-dortmund.de)

Received 21 February 2023, revised 16 May 2023

Accepted for publication 25 May 2023

Published 8 June 2023



CrossMark

## Abstract

Large area manufacturing processes of thin films such as large-area vacuum roll-to-roll coating of dielectric and gas permeation barrier layers in industry require a precise control of e.g. film thickness, homogeneity, chemical compositions, crystallinity and surface roughness. In order to determine these properties in real time, hyperspectral imaging is a novel, cost-efficient, and fast tool as *in-line* technology for large-area quality control. We demonstrate the application of hyperspectral imaging to characterize the thickness of thin films of the multilayer system ZTO/Ag/ITO produced by roll-to-roll magnetron sputtering on 220 mm wide polyethylene terephthalate substrate. X-ray reflectivity measurements are used to determine the thickness gradients of roll-to-roll produced foils with sub nanometer accuracy that serve as ground truth data to train a machine learning model for the interpretation of the hyperspectral imaging spectra. Based on the model, the sub-layer thicknesses on the complete substrate foil area were predicted which demonstrates the capabilities of this approach for large-scale *in-line* real-time quality control for industrial applications.

<sup>6</sup> These authors contributed equally.

\* Authors to whom any correspondence should be addressed.



Original content from this work may be used under the terms of the [Creative Commons Attribution 4.0 licence](https://creativecommons.org/licenses/by/4.0/). Any further distribution of this work must maintain attribution to the author(s) and the title of the work, journal citation and DOI.

Supplementary material for this article is available [online](#)

Keywords: hyperspectral imaging, x-ray reflectivity, machine learning, thickness prediction, thin films

(Some figures may appear in colour only in the online journal)

## 1. Introduction

Coating is the process of applying a thin layer of material to a substrate. This can be realized by deposition of a liquid-solution, for example in a spin-coating process with solvated metalorganics in solution, or vapor phases, for example in a sputtering process [1, 2] or atomic layer deposition. Depending on the application requirements, substrate material, coating parameters and coating technology are selected. In large-area coating techniques, especially in industry applications, a fast, efficient and very accurate quality control is necessary but its implementation is challenging.

A widely used coating method is the vacuum roll-to-roll (R2R) magnetron sputtering process. It is used to coat plastic substrates with thin films with a thickness in the nanometer range. For example, it can be applied in manufacturing processes for packaging foils with a gas permeation barrier for protection against water vapor and atmospheric gases, to manufacture metallic foils for the production of conductive surfaces [3], lacquer coatings and laminations between two glasses for low E-coatings for heat reflection and energy saving, electrochromic smart windows [4], or for flexible perovskite solar cells [5, 6]. Large scale industrial manufacturing of such functional coatings would benefit from an *in-line* quality control with real-time data analysis, requirements that can be addressed by application of hyperspectral imaging (HSI).

HSI is a method that collects a transmittance and/or reflectance spectrum from an illuminated object at each pixel in the camera image of a scene, hence it combines digital photography and spectroscopy. HSI is often performed in the visible and near-infrared spectral range (VNIR). HSI is routinely applied to many remote sensing usages, such as agriculture, waste sorting and recycling, surveillance, ocean monitoring, geology and astronomy [7–10]. It is a promising tool to access fast and accurate data during a manufacturing process in e.g. food, thin film and pharma industry for cost-efficient quality control [11–17]. Moreover, HSI has emerged in medical imaging, for example in detection of cancer tissue [18–20], Alzheimer disease biomarker [21] or ophthalmology [22, 23] and further diagnostic approaches [24, 25]. However, the commercial usage of HSI to characterize *in-situ* and in real-time large-area thin films during the production process still possess a major challenge. There is an inherent complexity in extracting the material's properties of interest such as e.g. the layer thickness, homogeneity, and crystallinity from the spectral intensity detected by each pixel.

There are two inherent challenges in the evaluation and use of HSI data: (i) the complex relationship between HSI spectra and sample properties requires physical modeling. Hence, evaluation of the measurements to obtain quantitative results

by an expert is needed, i.e. large personnel effort has to be invested. (ii) Due to the large amount of data, especially for R2R and *in-line* applications, a high computational effort has to be made. This concerns particularly cases where physical models must be applied to analyze each pixel of an HSI image. Here, soft modeling approaches with model training and live applications on incoming raw data and fast conversion are the key solutions. Addressing and optimizing such approach can lead to revolutionizing HSI machine designs for quality management in very different areas in industry [26], and may replace or support costly and complex downstream analytics that often provide no *in-line* production control.

In this manuscript, we report an approach for large-area thin film quality control that has the potential for application in industrial manufacturing processes for automated *in-line* thickness monitoring. We use x-ray reflectivity (XRR) to produce ground truth data of the layer thickness of a zinc tin oxide/silver/indium tin oxide (ZTO/Ag/ITO) layer system on polyethylene terephthalate (PET) manufactured by R2R magnetron sputtering in order to develop a prediction model for HSI spectra. We show how multimodal combination of XRR and HSI can be used to validate and refine a machine-learning model based on the partial least squares (PLSs) algorithm for prediction of film thicknesses.

## 2. Experimental

### 2.1. Multilayer fabrication and sample preparation

ZTO/Ag/ITO thin films on PET with a nominal thickness of 70 nm, 5 nm, and 40 nm, respectively, have been produced at Fraunhofer FEP (Dresden) using a vacuum web coater [27]. Figures 1(A) and (B) show the foil and a single cut out, part (C) sketch the multilayer system. The individual layers are applied to an unheated 125  $\mu\text{m}$  thick PET substrate (Melinex ST504, DuPont) by R2R magnetron sputtering of ceramic mixed targets with the nominal composition ZnO/SnO<sub>2</sub> (50.4/49.6 wt.%) and In<sub>2</sub>O<sub>3</sub>/SnO<sub>2</sub> (97/3 wt.%) in an Ar/O<sub>2</sub> mixture. The multilayers were produced over a width of 220 mm with web lengths up to 300 m. A part of the foil was extracted after the production process as shown in figure 1(A) and measured by HSI and XRR. For the XRR investigations, three pieces of the foil were cut out, laminated onto glass substrates (see colored areas in figure 1(A)) and each measured at five different positions by XRR. The XRR setup required a slightly different measurement geometry, i.e. rotation of the sample by 90°, for the measurements at the sample positions backward and forward in winding direction (see SI for details (figure S1)). The HSI measurements were performed on the full substrate area at  $\sim 200$  mm width. In the following we

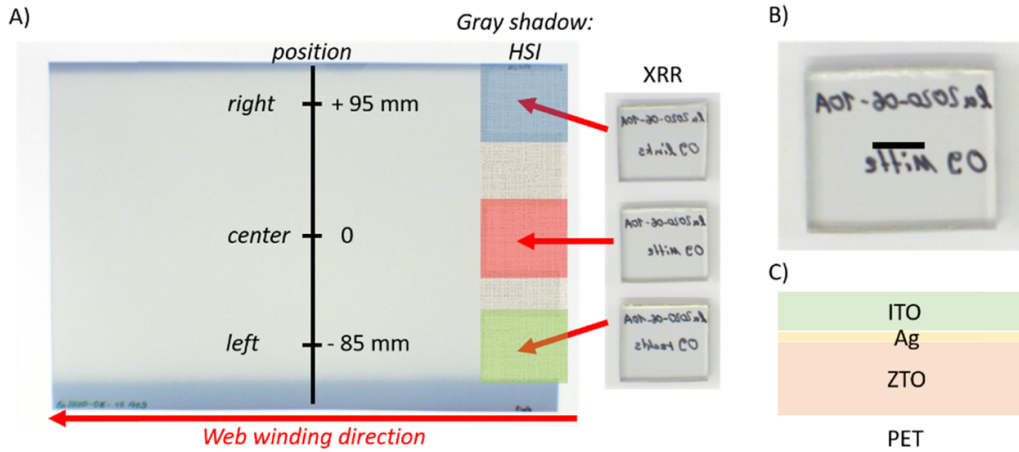


**Figure 1.** (A) Sample cut-outs from a part of the R2R foil for XRR sample preparation after HSI measurements of the shadowed gray area. The colors are used in figure 2 to represent the measurement location of the corresponding cut-out (blue = right, red = center, green = left). (B) Laminated sample with the black rectangle indicating the XRR measurement position of the central part and the dimensions of the beam footprint. (C) Schematic representation of the layer system.

will show exemplarily results obtained from the central part of each cut-out measured with XRR in more detail. This position is marked with a black rectangle in figure 1(B) showing a single laminated XRR sample.

## 2.2. XRR measurements and data analysis

XRR is an established and widely used technique for investigation of structural properties such as layer thickness, roughness, and electron density. It provides electron density profiles  $\rho(z)$  perpendicular to the layers' surface/interface with high resolution on an angstrom length scale. In such experiments, the reflected intensity of the sample surface is measured as a function of the angle of incidence  $\theta$  at specular condition, i.e. the angle of incidence is equal to the angle of reflection. Typically, the reflectivity data is presented as a function of the momentum transfer  $q_z$  perpendicular to the surface given by  $q_z = \frac{4\pi}{\lambda} \sin \theta$  with the wavelength  $\lambda$  of incident and reflected x-rays. The reflected intensity can be described by the first Born approximation [28] via

$$I(q_z) \propto \frac{1}{q_z^4} \left| \int \frac{d\rho(z)}{dz} \exp(iq_z z) dz \right|^2.$$

Thus this method is highly sensitive to changes of the electron density perpendicular to the sample surface ( $\frac{d\rho(z)}{dz}$ ) which allows to determine layer thicknesses of thin multilayer samples with highest precision. Consequently, XRR can be used to provide ground truth data for the training of machine learning models for the interpretation of HSI data. The HSI approach then can be applied to analyze lateral thickness gradients on a large scale.

The XRR data were measured at beamline BL9 of the synchrotron radiation source DELTA (Dortmund, Germany) [29, 30] using a photon energy of 8.048 keV which corresponds to wavelength of 1.54 Å with a beam size set to  $1 \times 0.1 \text{ mm}^2$  ( $h \times v$ ). A Pilatus 100K area detector (Dectris,

Switzerland) was utilized to measure both, the reflected intensity and the diffuse scattering for background subtraction simultaneously within a  $q_z$  range between 0.014 to 0.28 Å<sup>-1</sup>. The area probed by each XRR measurement is given by 1 mm perpendicular and on average about 8 mm parallel to the web winding direction which corresponds to approx. Six pixels and sixtyfour pixels of a hypercube in the HSI camera, respectively (see next section).

Each of the three laminated ZTO/Ag/ITO-covered PET samples (cut-outs) was investigated at five different positions on the samples, both perpendicular and parallel to the transport direction of the production process; please refer to the supplementary information (SI) figure S1 for more details. For data evaluation the XRR curves were normalized by the intensity of the incident radiation and then corrected by subtraction of the diffuse scattered intensity. Finally, the reflectivity data were evaluated with a combination of the Parratt algorithm [31] and the effective density model [32] using the program package LSFIT [33]. To minimize the number of fitting parameters, we initially assigned the literature electron density values [34] of ITO, Ag and ZTO to  $1.91 \text{ e}^- \text{ Å}^{-3}$ ,  $2.771 \text{ e}^- \text{ Å}^{-3}$  and  $1.642 \text{ e}^- \text{ Å}^{-3}$ , respectively, as starting parameters. Latter refers to a 3:2 Zn:Sn-ratio. The electron density of ZTO was determined from a separate XRR analysis of a ZTO single layer sample to  $1.62 \pm 0.05 \text{ e}^- \text{ Å}^{-3}$  and was fixed during the refinement in order to reduce the amount of variable fit parameters. The density of the PET substrate was set to the calculated value of  $0.44 \text{ e}^- \text{ Å}^{-3}$  and kept constant during the refinement while its roughness was fitted in the initial refinement loop and then fixed. We applied a three-layer-model to analyze the layer system on the PET substrate. A set of parameters was determined for each layer: the roughness ( $\sigma$ ), the thickness ( $d$ ) and the electron density ( $\rho$ ). The experimentally determined reflectivity curves together with the fit results are shown in figure 2(A) exemplarily for the central part of the three different cut-outs that are representative for a potential thickness gradient perpendicular to the transport



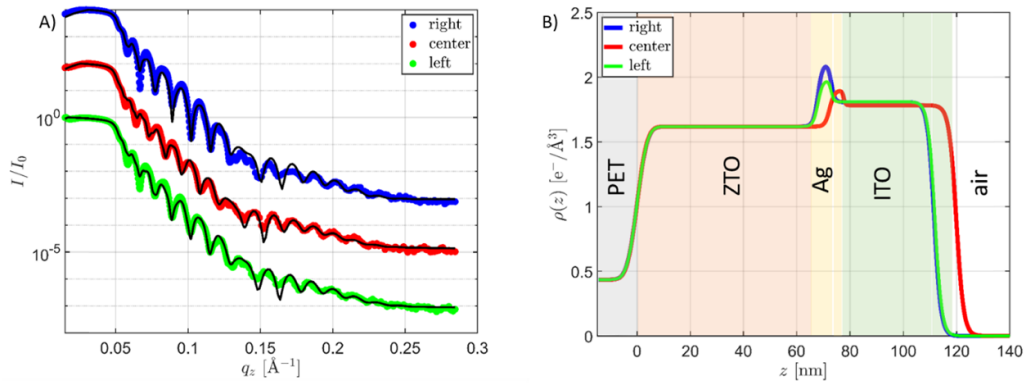


**Figure 2.** XRR data (A) of ZTO/Ag/ITO-coated PET foils measured at the central position of each extracted sample and corresponding electron density profiles (B). The XRR data is vertically shifted for clarity.

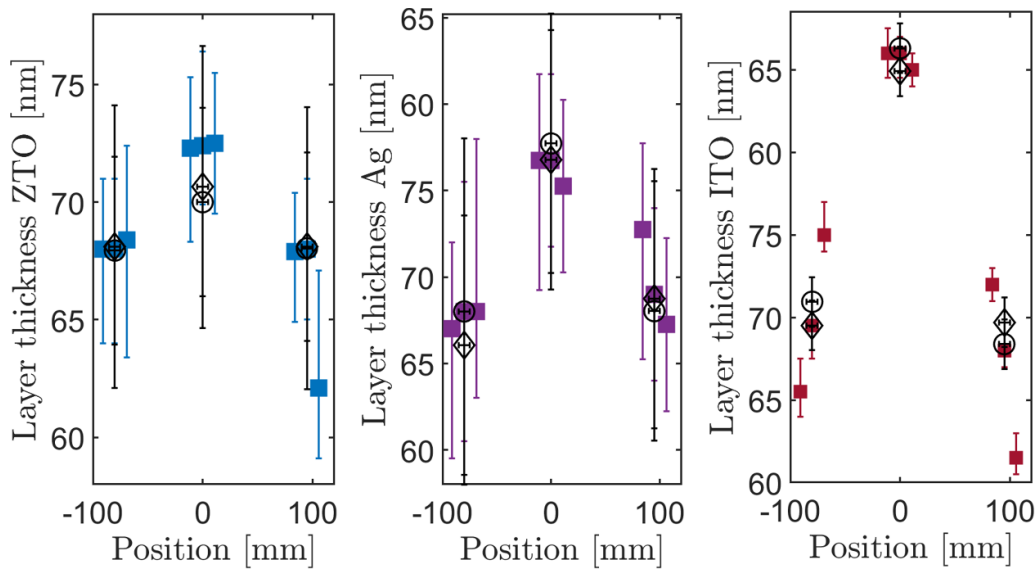


**Figure 3.** Layer gradients of the ZTO, Ag and ITO sublayers for different positions perpendicular to the transport direction. Open symbols show the layer thickness determined for positions before (diamonds) and behind (circle) the central part of each sample indicative for the homogeneity of the foil in transport direction. Please refer to the SI, figure S1, for visualization of the measurement positions on the samples. The errors are estimated via variation of the refinement parameters.

direction. One clearly observes that the reflectivities differ particularly regarding the oscillation period between the center sample and the ones extracted from the rims (left, right) of the foil. This is even more evident if the corresponding density profiles obtained from the fitting scheme are compared (see figure 2(B)) which show a significant decrease of the layer thickness of all sublayers to the rim of the foil. In web winding direction the sample is homogeneous as the XRR curves and density profiles hardly change (see figures S2–S4 in the SI). The thickness gradients of the sublayers are compiled in figure 3 including all measurements. The open symbols show the thicknesses determined parallel to the web winding direction which supports the thickness variation in that direction being much smaller. In contrast to the ZTO and the ITO layers, the density of the Ag layer is reduced by about 24% compared to the nominal Ag density. This indicates that the Ag layer is not fully closed but may show pore-like structure. All

extracted fit parameters are given in the SI (table S1). This data can be used as ground truth data to train and validate the machine learning models for interpretation of the HSI images and is applied in the following to the prediction of the layer thickness.

### 2.3. HSI

The HSI measurements were performed at the Fraunhofer IWS (Dresden, Germany) using a Headwall VNIR HSI camera (Headwall Photonics, USA) with  $1004 \times 1002$  sensor pixels, together with a Schneider Xenoplan  $f/1.4$  23 mm objective at an operating distance of 250 mm to the foil’s surface resulting in 100 mm field of view. The wavelengths detected by the camera range from 400 nm to 1000 nm.

A two times spatial and a four times spectral binning was used resulting in an effective pixel size of the camera of around

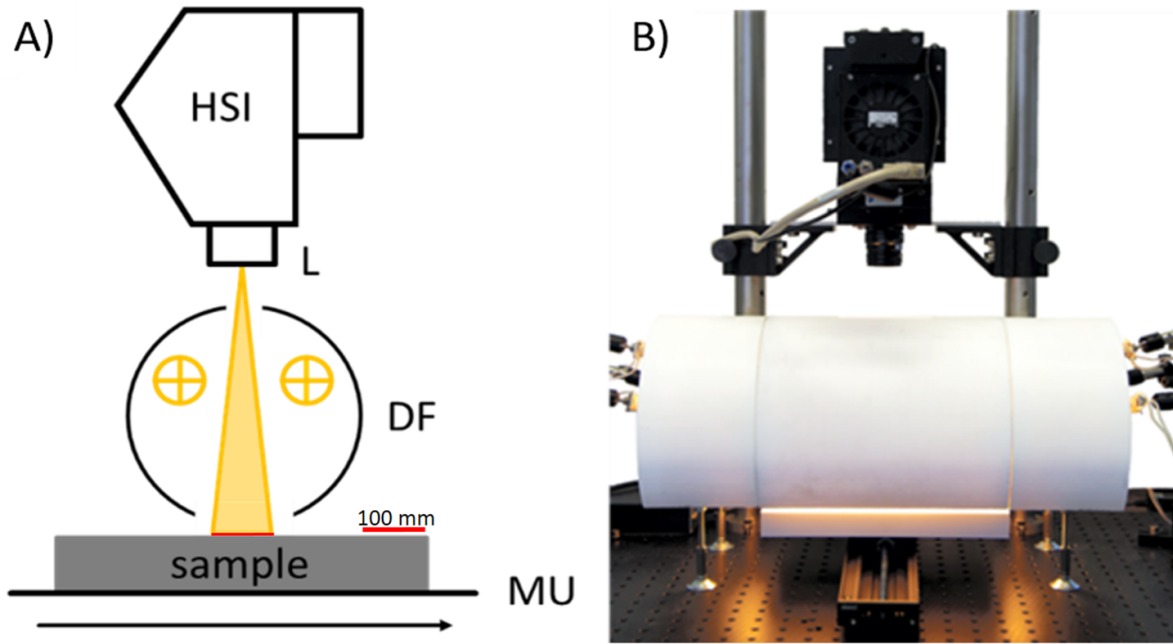


**Figure 4.** Schematic of the VNIR-HSI system (A) with the VNIR-HSI camera (HSI), lens (L), diffuse halogen illumination (DF) and motion unit (MU). Photo of the HSI system used (B).

170  $\mu\text{m}$  and a spectral resolution of around 4 nm. The foil was illuminated using a diffuse illumination system (Fraunhofer IWS, Dresden, Germany) with halogen lamps. The measurements were performed with the HSI software Imanto<sup>®</sup>pro (Fraunhofer IWS, Dresden, Germany) with a frame rate of 30 Hz and an exposure time of 25 ms. This exposure time at a given web speed of approximately 2 m  $\text{min}^{-1}$  results in a foil translation of less than 1 mm in web winding direction during one HSI measurement which determines the spatial averaging. This is in good agreement with the spatial resolution provided by the XRR measurements. Figure 4 shows a schematic drawing and a photo of the used HSI system.

To avoid irregularities in the lighting and to eliminate the influence of dark current, a white and a dark correction for each wavelength was carried out for the VNIR HSI measurement according to equation (1),

$$I_c(\lambda) = \frac{I_o(\lambda) - I_d(\lambda)}{I_w(\lambda) - I_d(\lambda)} \quad (1)$$

where  $I_c(\lambda)$  is the corrected image intensity,  $I_o(\lambda)$  the original image intensity,  $I_d(\lambda)$  is the dark current recorded with the light source switched off and the lens covered, and  $I_w(\lambda)$  is the intensity of the white reference for the wavelength  $\lambda$ . For the white reference, a plate of optical polytetrafluorethylene was scanned under the same measuring conditions as the original image. Since the specimen under study is a transparent film, a highly absorbing material (MaxiBlack Foil, Acktar Ltd, Israel) was placed under the specimen for the measurement to minimize a possible background effect. The measurement of the foil was performed before cutting it for XRR sample preparation. Figure 5 shows the result of the HSI measurement of the complete sample in terms of the color-coded reflectivity at a wavelength of 700 nm. The areas probed by the XRR

measurement and used for evaluating the ground truth data are indicated with blue stripes, each corresponding to around 100 spectra.

To obtain the training data for machine learning, the spectra in the marked stripes were selected and a mean spectrum was calculated. Because of the sample rotation in the XRR setup for selected sample positions in web winding direction, the orientation of the footprint area differs for these measurements as indicated in figure 5. However, inspection of the results presented in figure 3 shows that the layer thicknesses are not significantly affected by the footprint orientation so that we considered all data to train the model. Then, for each stripe, the most similar spectrum to the respective mean spectrum was selected. Figure 5 (right) shows the 15 spectra selected in this way. These 15 spectra and the corresponding layer thickness values from the XRR measurement could now be used in the next step for training machine learning regression models.

#### 2.4. Training and optimization of the PLS regression model for HSI thickness prediction

In the next step, a regression model was trained with the selected HSI spectra and the thicknesses for the Ag, the ITO and the ZTO layer determined from the XRR measurements in order to subsequently predict the layer thickness for the complete sample. The PLSs algorithm was chosen as the regression algorithm [35]. PLS is an algorithm used for regression analysis and dimensionality reduction. It is a supervised learning technique that finds a linear relationship between a response variable and one or more predictor variables by constructing a set of orthogonal latent variables that explain the maximum possible variance in both the predictor and response variables.

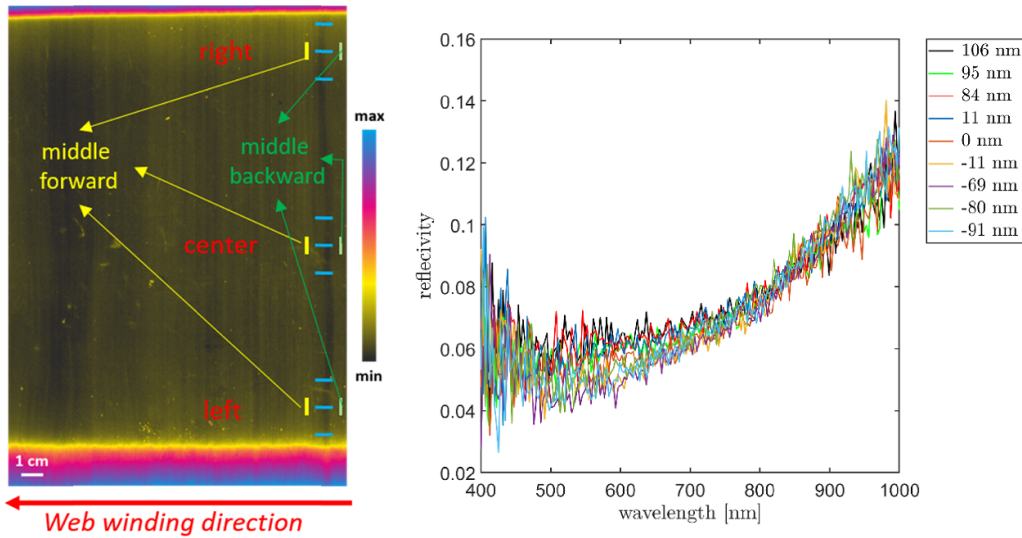


**Figure 5.** Result of the HSI measurement of the ZTO/Ag/ITO multilayer sample (left). The image shows the color-coded reflectivity (see equation (1)) measured at a wavelength of 700 nm. Here min and max refer to reflectivity values of 0.05 and 0.15, respectively. The areas probed by the XRR measurement and used for evaluation of the ground truth data are indicated with blue rectangles in standard measurement geometry and by yellow and green rectangles corresponding to a sample rotation by 90°. Selection of HSI spectra used for training of the machine learning regression model (right).

PLS is commonly used in fields such as chemistry and biology to analyze complex data sets and to build predictive models. Unlike other regression techniques, PLS can handle data sets with collinearity, missing values, and unbalanced design and it is particularly useful for modeling relationships between a response variable and a large number of predictor variables.

Before training the PLS model, optional preprocessing of the spectra by L1, L2 as spectrum division norm or standard normal variate normalization was performed. The type of preprocessing, as well as the number of latent variables (between 1 and 15) for the PLS were performed by automatic hyperparameter optimization using the random search algorithm [36]. For the hyperparameter optimization and the validation of the obtained models, a nested leave one out (LOO) cross validation was performed. To determine the quality and to compare the obtained regression models, the root mean square error (RMSE), the relative RMSE (rRMSE) and the coefficient of determination ( $R^2$ ) were analyzed. The RMSE is one of the most commonly used measures for evaluating the quality of predictions and shows how far predictions fall from measured true values using Euclidean distance. The determination was made for each of the outer cross-validation results. All model calculations were repeated three times and the mean and standard deviation for the metrics were determined. The calculations were performed with Python 3 and the library Scikit-learn [37].

### 3. Results and discussion

The results of the PLS regression model for the thickness of the three layers of the sample are shown in table 1. The results for the Ag and the ITO layer are comparable and provide an accurate prediction of the layer thickness confirmed by a

**Table 1.** Results of the PLS regression model for the prediction of the three layer thicknesses. All results were calculated by LOO cross validation. The standard deviation is obtained by repeating the model calculation three times.

	RMSE (nm)	rRMSE	$R^2$
Ag	$0.056 \pm 0.001$	$0.011 \pm 0.000$	$0.840 \pm 0.003$
ITO	$0.506 \pm 0.060$	$0.013 \pm 0.002$	$0.870 \pm 0.023$
ZTO	$1.204 \pm 0.014$	$0.018 \pm 0.000$	$0.515 \pm 0.001$

low RMSE, rRMSE and a high  $R^2$ . In contrast, the predictions of the ZTO layer thicknesses are worse, with an rRMSE more than double and an  $R^2$  of only 0.515. This is also reflected in the regression plots of the three models (see figure 6). The ZTO model shows the poorest fit, while the other models exhibit a remarkable correlation between the ground truth and the predicted thickness values. In order to assess the quality of the underlying ground truth data, error bars of the measured layer thicknesses are shown.

The results for the ZTO prediction deviate from the desired fit much stronger than for the other layers.

We trace this back to an increased model error due to the relatively large error of the ground truth data regarding the thickness determination by fitting the XRR curves. This is accompanied by a smaller variation in the training data. Most of the 15 positions investigated show the same ground truth layer thickness of about 68 nm. This makes a reasonable prediction in case of the ZTO layer questionable. It should also be noted that the differences between the HSI spectra of the different areas are relatively small and the spectra also have a low signal-to-noise ratio, which also complicates the training of the regression models. In addition, the measurement of the ZTO layer is complicated by the strongly deviating reflectivity

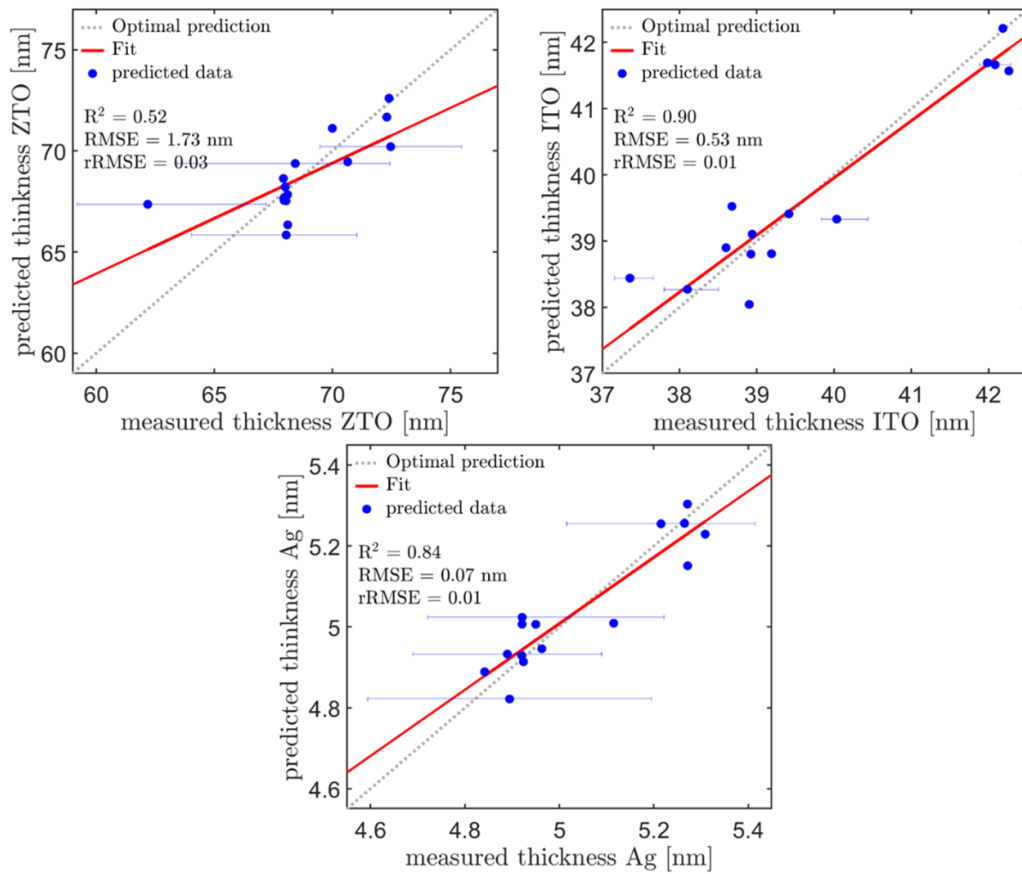


**Figure 6.** Regression plots for the best found PLS model for each of the three sublayers. The fit to the predicted data (points) is shown as red solid line while the optimal prediction is indicated as grey dotted line. The error bars of the layer thickness extracted from the measurements are given.

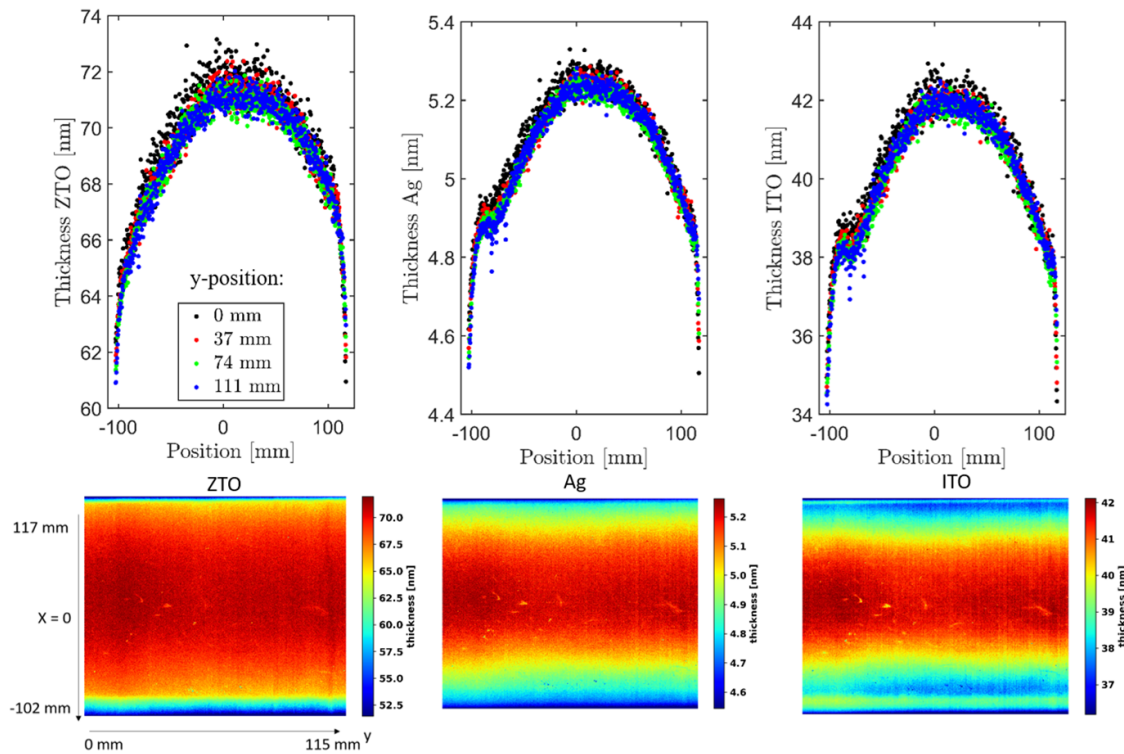


**Figure 7.** Predicted thickness distributions of the three sub-layers across the entire 220 mm wide PET substrate (bottom). Lateral thickness gradients compared for cross-sections perpendicular to the web-winding direction at different y-positions of the predicted images (top).



of the overlying Ag layer. Furthermore, the thicknesses of the three layers are strongly correlated with each other (see figure 3) and only a small thickness range is covered for all three coating materials. It can therefore be assumed that the models obtained cannot be generalized to arbitrary layer thickness combinations of ZTO/Ag/ITO. As only a few data points and no independent test samples could be examined in the present experiment, it can be assumed that the PLS model is overfitted which prevents a final conclusion on the predictive accuracy of the model for completely new samples.

Nevertheless, the models obtained were used to predict the thicknesses for the entire foil sample. For this purpose, the PLS models were applied to all spectra of the HSI measurement and the predicted film thicknesses were color coded. The results are shown in figure 7 (bottom). The same irregularities can be observed in all three images. These are artifacts attributed to substrate imperfections like surface contaminations and dust before coating. In the top part of the figure we present cross-sections perpendicular to the web-winding direction at different y-positions of the predicted image in order to compare the predicted layer gradients for the position where the ground truth data were measured (111 mm) with the predictions at other parts of the foil. Again, the strong correlation of the sub-layer thicknesses can be recognized, with the layer thickness distribution for the ZTO layer differing slightly from the distribution of the Ag and ITO layers. However, the model is capable to provide reasonable thickness gradients for the complete sample. Despite the deficiencies on predicting the ZTO layer thickness with highest accuracy compared to the Ag and ITO layers, the detection of film thicknesses using HSI over a foil width of 220 mm for such a complex layer system is remarkable. For evaluation of the HSI data, analysis of one spectrum using the trained prediction model is in the range of some milliseconds. The prediction of the whole image takes below 5 s which provides reasonable reaction times in case of production failure. These results validate the capabilities of the presented approach for accurate *on-line* thickness control of multilayer coatings although a larger ground truth data base is required which needs to cover large thickness gradients for a generalization of such models to various layer systems.

#### 4. Conclusion

In summary, we conclude that the presented method is well suited for the complete and fast thickness prediction of thin film samples via HSI using models that are trained using a relatively small amount of ground truth data obtained by XRR measurements. In future, a combination of HSI measurements and XRR as ground truth data source could provide a rapid thickness prediction for various materials by using libraries of pre-trained machine learning models. The present approach is especially suited to determine thickness variations of large-area samples which is of utmost relevance for industrial production processes. In fact, we have recently succeeded to model and predict film thicknesses in the sub-100 nm range for a web width of 300 mm and a web speed of  $2 \text{ m min}^{-1}$ . The concept could also be extended to other layer properties that

are accessible by XRR such as density or roughness or different type of ground truth data e.g. the crystallinity and phase composition of thin films determined by x-ray diffraction.

#### Data availability statement

All data that support the findings of this study are included within the article (and any supplementary files).

#### Acknowledgments

The research has been carried out within the NanoQI project which has received funding from the European Union's Horizon 2020 research and innovation programme under Grant Agreement No. 862055. We thank Stefan Jacobs (Bruker AXS) for discussions and training concerning XRR evaluation strategies. DELTA at TU Dortmund is acknowledged for providing synchrotron radiation at beamline BL9.

#### Contributions

S C, F G, P W, M T and C S designed the research. All ZTO/Ag/ITO samples were produced and prepared at Fraunhofer FEP with support by P S. P W and C M implemented the HSI camera and the local XRR system used for on-site thickness determination, respectively, and provided user support. F G and P W performed the HSI measurements. S C and P S performed and analyzed lab XRR measurements on ZTO and ITO reference single layers. S B, S D S, C A, E S, N T, M P and C S performed the XRR measurements at beamline BL9 of DELTA. S B analyzed the XRR measurements with help of S D S and M P. F G and P W analyzed the HSI spectra, trained, optimized and validated the machine learning models. S D S, F G and C S wrote the manuscript with contributions from all coauthors.

#### ORCID iDs

Susanne Dogan-Surmeier  <https://orcid.org/0000-0003-2140-3047>

Florian Gruber  <https://orcid.org/0000-0001-9405-797X>

Christian Albers  <https://orcid.org/0000-0002-0526-0675>

Nicola Thiering  <https://orcid.org/0000-0002-9337-5260>

Philipp Wollmann  <https://orcid.org/0000-0002-4473-9750>

Christian Sternemann  <https://orcid.org/0000-0001-9415-1106>

#### References

- [1] Butt M A 2022 Thin-film coating methods: a successful marriage of high-quality and cost-effectiveness—a brief exploration *Coatings* **12** 1115
- [2] Krebs F C 2009 Fabrication and processing of polymer solar cells: a review of printing and coating techniques *Sol. Energy Mater. Sol. Cells* **93** 394–412
- [3] Palavesam N, Marin S, Hemmetzberger D, Landesberger C, Bock K and Kutter C 2018 Roll-to-roll processing of film

- substrates for hybrid integrated flexible electronics *Flex. Print. Electron.* **3** 014002
- [4] Lin S et al 2017 Roll-to-roll production of transparent silver-nanofiber-network electrodes for flexible electrochromic smart windows *Adv. Mater.* **29** 1703238
- [5] Zi W, Jin Z, Liu S and Xu B 2018 Flexible perovskite solar cells based on green, continuous roll-to-roll printing technology *J. Energy Chem.* **27** 971–89
- [6] Dou B et al 2018 Roll-to-roll printing of perovskite solar cells *ACS Energy Lett.* **3** 2558–65
- [7] Wang L and Zhao C 2016 Introduction of hyperspectral remote sensing applications *Hyperspectral Image Processing* ed L Wang and C Zhao (Berlin: Springer) pp 283–308
- [8] Rhoby M R, Blunck D L and Gross K C 2014 Mid-IR hyperspectral imaging of laminar flames for 2D scalar values *Opt. Express* **22** 21600–17
- [9] Pasquini L, Avila G, Blecha A, Cacciari C, Cayatte V, Colless M, Damiani F, De Propriis R, Dekker H and Di Marcantonio P 2002 Installation and commissioning of FLAMES, the VLT multifibre facility *Messenger* **110** 1–9
- [10] Risse S et al 2019 Ultraprecise flat mirrors for the pointing unit of the DESIS instrument on board of the ISS vol 11101
- [11] He J, Liu Y, Li Z, Ji Z, Yan G, Zhao C and Mai W 2022 Achieving dual-color imaging by dual-band perovskite photodetectors coupled with algorithms *J. Colloid Interface Sci.* **625** 297–304
- [12] Gebauer J, Gruber F, Holfeld W, Grählert W and Lasagni A F 2022 Prediction of the quality of thermally sprayed copper coatings on laser-structured CFRP surfaces using hyperspectral imaging *Photonics* **9** 439
- [13] Stranzinger S, Wolfgang M, Klotz E, Scheibelhofer O, Ghiotti P, Khinast J G, Hsiao W-K and Paudel A 2021 Near-infrared hyperspectral imaging as a monitoring tool for on-demand manufacturing of inkjet-printed formulations *AAPS PharmSciTech* **22** 6
- [14] Gerdes N, Hoff C, Hermsdorf J, Kaieler S and Overmeyer L 2021 Hyperspectral imaging for prediction of surface roughness in laser powder bed fusion *Int. J. Adv. Manuf. Technol.* **115** 1249–58
- [15] Frosch T, Wyrwich E, Yan D, Popp J and Frosch T 2019 Fiber-array-based Raman hyperspectral imaging for simultaneous, chemically-selective monitoring of particle size and shape of active ingredients in analgesic tablets *Molecules* **24** 4381
- [16] Liu Y, Pu H and Sun D-W 2017 Hyperspectral imaging technique for evaluating food quality and safety during various processes: a review of recent applications *Trends Food Sci. Technol.* **69** 25–35
- [17] Yoon C, Park G, Han D, Im S-I, Jo S, Kim J, Kim W, Choi C and Lee M 2022 Toward realization of high-throughput hyperspectral imaging technique for semiconductor device metrology *J. Micro/Nanopatterning Mater. Metrol.* **21** 2
- [18] Lu G and Fei B 2014 Medical hyperspectral imaging: a review *J. Biomed. Opt.* **19** 010901
- [19] Collins T et al 2022 Automatic optical biopsy for colorectal cancer using hyperspectral imaging and artificial neural networks *Surg. Endosc.* **36** 8549–59
- [20] Kong S G, Martin M E and Vo-Dinh T 2006 Hyperspectral fluorescence imaging for mouse skin tumor detection *ETRI J.* **28** 770–6
- [21] Hadoux X et al 2019 Non-invasive *in vivo* hyperspectral imaging of the retina for potential biomarker use in Alzheimer's disease *Nat. Commun.* **10** 4227
- [22] Li H, Liu W, Dong B, Kaluzny J V, Fawzi A A and Zhang H F 2017 Snapshot hyperspectral retinal imaging using compact spectral resolving detector array *J. Biophoton.* **10** 830–9
- [23] Johnson W R, Wilson D W, Fink W, Humayun M and Bearman G H 2007 Snapshot hyperspectral imaging in ophthalmology *JBO* **12** 014036
- [24] Alafeef M and Pan D 2022 Diagnostic approaches for COVID-19: lessons learned and the path forward *ACS Nano* **16** 11545–76
- [25] Sucher R et al 2022 Hyperspectral imaging (HSI) of human kidney allografts *Ann. Surg.* **276** e48
- [26] Chandran Suja V, Sentmanat J, Hofmann G, Scales C and Fuller G G 2020 Hyperspectral imaging for dynamic thin film interferometry *Sci. Rep.* **10** 11378
- [27] Steiner C, Fahlteich J and Rädlein E 2015 Nanostructuring of ethylene tetrafluoroethylene films by a low pressure plasma treatment process
- [28] Als-Nielsen J and McMorrow D 2011 *Elements of Modern X-Ray Physics* (New York: Wiley)
- [29] Tolan M, Weis T, Westphal C and Wille K 2003 DELTA: synchrotron light in Nordrhein-Westfalen *Synchrotron. Radiat. News* **16** 9–11
- [30] Paulus M, Lietz D, Sternemann C, Shokuie K, Evers F, Tolan M, Czeslik C and Winter R 2008 An access to buried interfaces: the x-ray reflectivity set-up of BL<sub>9</sub> at DELTA *J. Synchrotron Radiat.* **15** 600–5
- [31] Parratt L G 1954 Surface studies of solids by total reflection of x-rays *Phys. Rev.* **95** 359
- [32] Tolan M 1999 *X-ray Scattering from Soft-Matter Thin Films: Materials Science and Basic Research* (Berlin: Springer)
- [33] Seeck O H, Kaendler I D, Tolan M, Shin K, Rafailovich M H, Sokolov J and Kolb R 2000 Analysis of x-ray reflectivity data from low-contrast polymer bilayer systems using a Fourier method *Appl. Phys. Lett.* **76** 2713–5
- [34] Henke B L, Gullikson E M and Davis J C 1993 X-ray interactions: photoabsorption, scattering, transmission, and reflection at E=50–30000 eV, Z=1–92 *At. Data Nucl. Data Tables* **54** 181–342 (CXRO - The Center for X-Ray Optics)
- [35] Geladi P and Kowalski B R 1986 Partial least-squares regression: a tutorial *Anal. Chim. Acta* **185** 1–17
- [36] Bergstra J and Bengio Y 2012 Random search for hyper-parameter optimization *J. Mach. Learn. Res.* **13** 281–305
- [37] Pedregosa F, Varoquaux G, Gramfort A, Michel V, Thirion B, Grisel O, Blondel M, Prettenhofer P, Weiss R and Dubourg V 2011 Scikit-learn: machine learning in Python *J. Mach. Learn. Res.* **12** 2825–30